Supersonic wave propagation in active non-Hermitian acoustic metamaterials

Kangkang Wang,[1] Felix Langfeldt,[2,*] Chen Shen,[3] Haishan Zou,[1] Sipei Zhao,[4] Jing Lu,[1,†] and Lea Sirota[5,‡]

[1]*Key Laboratory of Modern Acoustics, MOE, Institute of Acoustics, Department of Physics, Nanjing University, Nanjing 210093, P. R. China*
[2]*Institute of Sound and Vibration Research, University of Southampton, University Road, Highfield, Southampton, SO17 1BJ, United Kingdom*
[3]*Department of Mechanical Engineering, Rowan University, Glassboro, NJ 08028, USA*
[4]*Centre for Audio, Acoustics and Vibration, Faculty of Engineering and IT, University of Technology Sydney, Ultimo, NSW 2007, Australia*
[5]*School of Mechanical Engineering, Tel Aviv University, Tel Aviv 69978, Israel*

Obtaining a group velocity higher than the speed of sound in a waveguide is a challenging task in acoustic wave engineering. Even more challenging is to achieve this velocity increase without any intervention with the waveguide profile, such as narrowing or widening, and particularly without interfering with the passage by flexible inclusions, either passive or active. Here, we approach this problem by invoking concepts from non-Hermitian physics, and imposing them using active elements that are smoothly sealed within the waveguide wall. In a real-time feedback operation, the elements induce local pressure gain and loss, as well as non-local pressure integration couplings. We employ a dedicated balancing between the control couplings, derived from lattice theory and adjusted to the waveguide system, to drive the dynamics into a stable parity-time-symmetric regime. We demonstrate the accelerated propagation of a wave packet both numerically and experimentally in an air-filled waveguide, and discuss the trade-off between stabilization and the achievable velocity increase. Our work prepares the grounds for advanced forms of wave transmission in continuous media, enabled by short and long range active couplings, created via embedded real-time feedback control.

I. INTRODUCTION

Non-Hermitian systems, where interactions and exchange of energy with the surrounding environment are allowed, have been shown to exhibit unique properties in recent years[1,2]. Their effective non-Hermitian Hamiltonians endow exceptional properties and topologies that go beyond conventional Hermitian counterparts. A prime example is parity-time (PT) symmetry and the emergence of exceptional points (EPs), which has garnered great research interest[3,4]. The eigenvalues and eigenstates of these PT-symmetric systems coalesce in the parameter space, and real eigenvalues are possible with complex Hamiltonians. Initially a purely mathematical model[5,6], the concept was later successfully tested in photonic systems with balanced loss and gain potentials thanks to the equivalence between the paraxial electromagnetic wave equation and the Schrödinger equation[7]. Since then, numerous PT-symmetry and EP-related effects have been discovered, which suggested new functionalities and applications by tailoring the complex energy profile of the systems under study, including single-mode lasers[8], enhanced sensitivity[9], unidirectional invisible cloaking[10,11], and so on.

In the field of acoustics and elastodynamics, researchers have studied similar concepts and revealed a plethora of intriguing phenomena[12–18]. Because of the absence of natural gain materials, a common approach is implementing an equivalent model with only lossy or lossless media, leaving part of the parameter space untapped. Although these systems are successful in terms of constructing a complex effective Hamiltonian, recent studies have suggested that certain effects can only be induced by real gain-loss modulations[19–21]. The use of gain media introduces external energy and broadens the utility of the parameter space. Several previous attempts have implemented real gain media using different techniques, such as electro-thermoacoustic coupling[22,23], background airflow[24], energy injection[25,26], or active control elements[27,28]. Nevertheless, the non-Hermitian phenomena demonstrated so far have been focused mostly on the property of nonreciprocity, and less on the control of wave propagation velocity. In addition, the common realizations of active couplings, in particular in acoustic waveguides, involve either alternations of the waveguide geometry, or placement of the actuators at the waveguide cross-section[27,29,30].

In this work, we address spatially continuous media, such as acoustic waveguides, hybridized with discretely-spanned active elements, which are seamlessly embedded in the waveguide wall. We program these elements to actively control the wave propagation velocity in a plain waveguide with a uniform cross-section. This is useful for applications for which the passage of fluid through the waveguide cannot be blocked. Motivated by control schemes for purely discrete PT-symmetric media, such as lattices[31,32], we derive the required couplings to speed-up wave packet propagation in the waveguide. Specifically, the active units control the onsite loss and gain profiles, as well as the internal couplings between the units, to create an effective PT-symmetric system. Utilizing the concept of feedback-based media[30,33? –40], we realize these couplings in a real-time closed loop process.

At the first stage, we develop a theoretical model to describe the system and study the impact of different parameters on the propagation characteristics of the waves, which is further validated by finite element simulations. The results suggest that despite the dynamical difference between purely discrete and hybrid continuous-discrete structures due to the inevitable responses between the sites of the latter, such as time delays, near field effects, etc., a faster group velocity compared to the background medium is possible in the waveguide system with judiciously tailored modulation profiles.

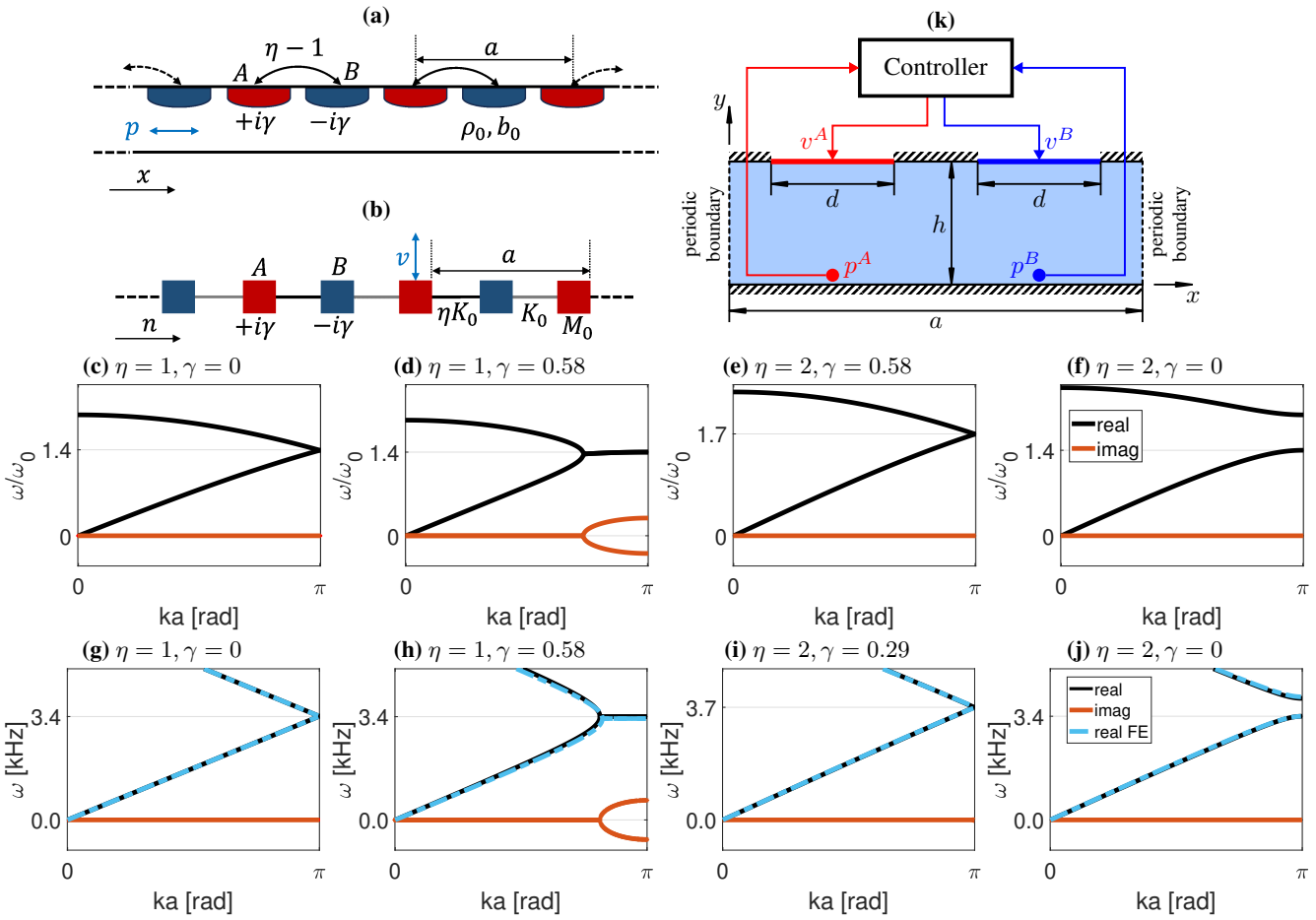

FIG. 1. The active acoustic metamaterial model and its spectral properties. (a) The waveguide schematics. (b) Analogous lattice schematics. (c)-(f) Frequency dispersion of an infinite lattice system. (c) Nominal stable, $\gamma = 0, \eta = 1$. (d) Unstable, $\gamma = 0.58, \eta = 1$. (e) PT-symmetry-restored stable, $\gamma = 0.58, \eta = 2$. (f) Controlled stable, $\gamma = 0, \eta = 2$. (g)-(j) Frequency dispersion of an infinite waveguide system at low frequencies ($\beta = 1$). (g) Nominal stable, $\gamma = 0, \eta = 1$. (h) Unstable, $\gamma = 0.58, \eta = 1$. (i) PT-symmetry-restored stable, $\gamma = 0.29, \eta = 2$. (j) Controlled stable, $\gamma = 0, \eta = 2$. (k) Sketch of the finite element (FE) model setup for numerically calculating the dispersion curves.

Owing to the central role that stability plays in actively controlled wave systems[41], we derive the criteria for stable wave propagation in the metamaterial so that wave amplitude is not growing during the propagation. We confirm our theoretical predictions of obtaining a group velocity higher than the speed of sound in air by carrying out experiments in an acoustic waveguide. Our results showcase the implementation of active acoustic wave control in combination with PT-symmetry to support stable faster-than-sound dynamic pulse transmission. The work facilitates the spatio-temporal modulation of signals with real-time tuning capabilities and may find applications in acoustic communication and more.

II. THE TARGET WAVEGUIDE MODEL

We consider an acoustic waveguide that supports propagation of sound pressure waves p in a fluid of mass density ρ_0 and bulk modulus b_0, as illustrated in Fig. 1(a). Active elements are connected to the waveguide wall in a periodic spacing a, and facing inwards. The elements, labeled by A and B, respectively induce local gain $+\mathrm{i}\gamma$ and loss $-\mathrm{i}\gamma$, as well as an additional coupling $\eta - 1$ between each A-B pair. The actively controlled waveguide thus constitutes a hybrid continuous-discrete medium. The role of the active elements is to increase the wave group velocity inside the waveguide, v_g, beyond the background speed of sound c. As the wave propagation must be dynamically stable, i.e., with non-growing amplitudes, it is required to derive a relation between the parameters γ and η so that two conditions hold: $v_g > c$, and the system's stability is preserved.

We then consider an auxiliary model, an analogous mass-spring lattice, which is inherently discrete, Fig. 1(b), and derive the $\gamma - \eta$ relation for this model first. Each lattice site has a single degree of freedom, i.e., the vertical displacement y. The masses M_0 and spring constants K_0 are analogous to the mass density and bulk modulus of the fluid as $M_0 = \rho_0 a S_0$ and $K_0 = b_0 S_0 / a$, where S_0 is the waveguide cross-section, and the velocity $v = \dot{y}$ maps to the pressure p. The coupling ηK_0 may then be regarded as a different spring constant, and the loss (gain) $\mp\mathrm{i}\gamma Z_0$ as an onsite viscous damper (anti-damper) connected to ground, where $Z_0 = \sqrt{M_0 K_0}$ is the mechanical impedance. The dynamics of the n_{th} A and B

sites of the dimer lattice can be formulated as

$$\omega_0^{-2}\ddot{y}_n^{A/B} = y_{n\mp1}^{B/A}+\eta y_n^{B/A}-(1+\eta)y_n^{A/B}\pm\gamma\omega_0^{-1}\dot{y}_n^{A/B}, \quad (1)$$

where $\omega_0 = \sqrt{K_0/M_0}$. We insert the solution $\begin{bmatrix} y_n^A & y_n^B \end{bmatrix}^T = \begin{bmatrix} \overline{y}^A & \overline{y}^B \end{bmatrix}^T e^{\mathrm{i}(kna-\omega t)}$ in Eq. (1) , where k is the wavenumber, and $\overline{y}^A, \overline{y}^B$ are the respective wave amplitudes. Defining the normalized frequency $\Omega = \omega/\omega_0$, we then obtain the augmented eigenvalue problem $(\Omega\mathbf{I} - \mathcal{H})\,\overline{\mathbf{y}} = \mathbf{0}$, with the augmented eigenvector $\overline{\mathbf{y}}$ including $\overline{y}^A$, $\overline{y}^B$, and two auxiliary states. The effective 4×4 Hamiltonian $\mathcal{H}$ is given by

$$\mathcal{H} = \begin{pmatrix} \mathbf{0} & \mathbf{I} \\ \mathcal{H}_0 + (1+\eta)\mathbf{I} & \mathrm{i}\gamma\boldsymbol{\sigma}_z \end{pmatrix}, \; \mathcal{H}_0 = \begin{pmatrix} 0 & f \\ f* & 0 \end{pmatrix}, \quad (2)$$

where $f = -\left[\eta + e^{-\mathrm{i}ka}\right]$ and $\boldsymbol{\sigma}_z$ is the Pauli matrix. For general η and γ this Hamiltonian is non-Hermitian[1]. The solution of the eigenvalue problem in (2) gives the lattice dispersion relation, and consequently the required relation between γ and η for dynamical stability[32]. This is illustrated in Fig. 1(c)-(f). For the nominal lattice, i.e. for $\gamma = 0$ and $\eta = 1$, the spectrum is purely real, as expected, Fig. 1(c), where the top band is idle (due to the lattice constant folding to $a/2$). When increasing γ, for example to 0.58, the spectrum becomes complex-valued around the band crossing point, turning it into an exceptional cut[4], Fig. 1(d). The time response at the n_{th} node then takes the form $y_n(t) \propto e^{\omega_I t}e^{\mathrm{i}(kna-\omega_R t)}$, where ω_R and ω_I are the real and imaginary components of the frequency, respectively. The response thus grows unbounded, indicating the system's dynamical instability.

For the particular relation $\gamma^* = \sqrt{2}\left(\sqrt{\eta}-1\right)$, the lattice spectrum is restored to be purely real, as illustrated in Fig. 1(e) for $\eta = 2$ and $\gamma = 0.58$, while preserving the non-Hermiticity of the Hamiltonian (2). This transition indicates the restoration of the PT-symmetric phase. For any $\gamma < \gamma^*$ the spectrum remains real, albeit gapped, Fig. 1(f), thus forming the lattice stability region in the $\gamma-\eta$ plane. Remarkably, the new crossing point of the dispersion curves for $\gamma = \gamma^*$, which is an exceptional point, occurs at a higher frequency than for the nominal case, indicating an increase in group velocity. This increase is given by $v_g = v_0\sqrt{\frac{1}{\sqrt{2}}\gamma^*+1}$, suggesting that it is possible to exceed the Hermitian group velocity v_0, and at the same time to guarantee dynamical stability (see App. A).

Inspired by the results for the lattice system, we now aim at deriving analogous results for the actual waveguide. We create the γ and η couplings using feedback control loops involving the active elements in Fig. 1(a). These elements, positioned at x_n, produce acoustic control velocities v_n, and are incorporated in the field equation as

$$\frac{1}{c^2}p_{tt}(x,t) = p_{xx}(x,t) + \rho_0\beta\sum_n \dot{v}_n(t)\delta(x-x_n), \quad (3)$$

where c is the speed of sound in air, $\delta(\cdot)$ indicates the location of the relevant coupling along the x axis, and β is the ratio between the active element area S_a and the waveguide cross-section S_0. To generate closed loop dynamics analogous to (1), the velocity inputs at the A and B sites take the form

$$v_n^{A/B}(t) = \frac{\eta-1}{\rho_0 a}\int_0^t [p_n^{B/A}(t) - p_n^{A/B}(t)]\mathrm{d}t \pm \frac{\gamma}{z_0}p_n^{A/B}(t), \quad (4)$$

where $p_n^{A/B}(t)$ is a compact form of $p(x_n^{A/B},t)$, and $z_0 = \rho_0 c$ is the specific acoustic impedance. In closed loop, the waveguide supports faster-than-sound wave propagation, obeying

$$\begin{aligned} &\frac{1}{c^2}p_{tt}(x,t) = p_{xx}(x,t) \\ &+\beta\sum_n \frac{\eta-1}{a}(p_n^B(t)-p_n^A(t))\delta(x-x_n^A) \\ &+\beta\sum_n \frac{\eta-1}{a}(p_n^A(t)-p_n^B(t))\delta(x-x_n^B) \\ &+\beta\frac{\gamma}{c}\sum_n \left[\dot{p}_n^A(t)\delta(x-x_n^A) - \dot{p}_n^B(t)\delta(x-x_n^B)\right], \end{aligned} \quad (5)$$

(see App. B). We calculate the dispersion of Eq. (5) using the plane wave expansion (PWE) method[42], in which a series solution of traveling harmonic waves, $p(x,t) = \mathrm{e}^{-\mathrm{i}\omega t}P(x)$, is assumed, where $P(x) = \sum_{m=-M}^{M}\mathrm{e}^{\mathrm{i}(k+m)\mathbf{b}_1\cdot x\mathbf{d}_1}\overline{p}$. $\mathbf{b}_1 = \frac{2\pi}{a}\hat{\mathbf{e}}_1$ and $\mathbf{d}_1 = a\hat{\mathbf{e}}_1$ respectively span the momentum and the real spaces, $\overline{p}$ is the pressure field amplitude, and M is the approximation order (see App. C). Due to the continuity of the acoustic medium there is an infinite number of bands, where M that we choose for the calculation defines how many of these bands are plotted. The resulting spectrum is depicted in Figs. 1(g)-(j) in low frequencies for an air -filled waveguide. The waveguide cross-sectional area is assumed equal to that of the active elements, i.e. $\beta = 1$, with a spacing of $a = 5$ cm, and $M = 4$.

Fig. 1(g) depicts the spectrum of the uncontrolled waveguide. The crossing point of the main band with its folding, which occurs at $ka = \pi$, directly implies the slope of 343 m/s, which, as expected, equals c, the speed of sound in air. We then begin to increase γ while keeping $\eta = 1$. Similarly to the lattice system, an imaginary spectrum appears, as depicted in Fig. 1(h) for $\gamma = 0.58$. To eliminate the imaginary spectrum we increase η as well. For $\eta = 2$, the balance is obtained for $\gamma = 0.29$, as shown in Fig. 1(i). In the general case, we obtain the balancing formula for the waveguide, and the corresponding group velocity, as

$$\gamma^* = \tfrac{1}{\sqrt{2}}\left(\sqrt{\eta}-1\right)\mu, \quad v_g = v_0\sqrt{\beta\tfrac{1}{\sqrt{2}}\gamma^*+1}, \quad (6)$$

where μ is a small fine-tuning term required for higher values of η, and/or $\beta < 1$. Decreasing γ below the relation in Eq. (6) keeps the spectrum real, albeit gapped, as in the lattice, as illustrated in Fig. 1(j) for $\eta = 2$ and $\gamma = 0$. The waveguide stability criterion in Eq. (6) is slightly different from the lattice criterion, resulting in smaller gain/loss values for a given η. There might be several reasons for this, including the inherent differences between discrete and hybrid continuous/discrete systems, the fact that we attach the active elements only to one of the waveguide walls, and more. The resulting group velocity increase follows a similar law as for

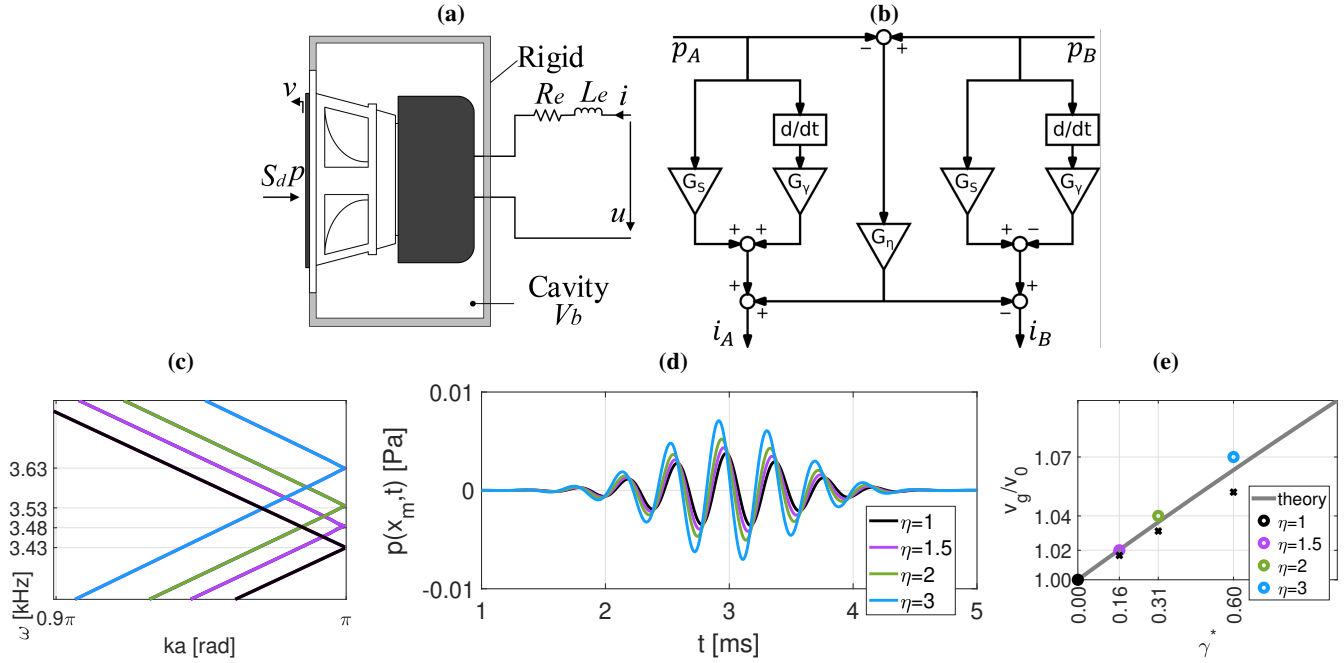

FIG. 2. Waveguide realization in a feedback control setup using current driven electroacoustic transducers. (a) Schematic of the electrodynamic speaker driven by a 2.5 kHz current source. (b) The controller structure. (c) The waveguide dispersion relation obtained from PWE for $a = 5$ cm and $\beta = 0.32$, featuring the uncontrolled case $\gamma = 0, \eta = 1$ (black), and the controlled cases $\gamma = 0.16, \eta = 1.5$ ($\sigma = 1$) (purple), $\gamma = 0.31, \eta = 2$ ($\sigma = 1.055$) (green), and $\gamma = 0.60, \eta = 3$ ($\sigma = 1.161$) (blue). (d) Time domain responses calculated via FE. (e) The normalized group velocities obtained from the time domain simulations (circles), plotted on top of the analytic expression Eq. (6) (gray).

the lattice. This implies that in order to achieve a required v_g, the same γ as in the lattice balances a stronger coupling η in the waveguide. For example, $\gamma = 0.58$ balances $\eta = 3.42$.

To confirm the results obtained via the PWE, we calculate the waveguide's frequency dispersion using finite element (FE) analysis. As shown in Fig. 1(k), the domain is modeled as two-dimensional, representing a cross-section of the waveguide with the main propagation axis x and the vertical axis y. The height of the waveguide h and the actuator length d are explicitly included in the model. The actuators are represented by velocity sources and point probes are used at the waveguide wall opposite to the actuators (similar to the experimental setup, described in Sec. IV) to obtain the pressures p^A and p^B. Using these pressure values, the control law given in Eq. (4) is implemented to drive the velocity sources and create the required couplings. The ends of the waveguide section of length a, representing one unit cell, are terminated using periodic boundary conditions. All other boundaries are set to be sound hard. The dispersion curves were calculated by computing the eigenvalues of the system with different ka values prescribed at the periodic boundary conditions. The results are depicted in Fig. 1(g)-(j) in dashed cyan on top of the PWE results. The FE and the PWE results nearly coincide.

III. CONTROLLER DESIGN

Since it is not possible to directly impose acoustic velocity, we realize the control velocity sources using electroacoustic transducers, specifically by electrodynamic loudspeakers, which replace the ideal actuators in Fig. 1(k). The control setup of each unit cell then consists of two speakers, which generate control velocities v_A and v_B, as well as two microphones, which measure the pressure signals p_A and p_B. Based on these measurements, the actuators create the $+\mathrm{i}\gamma$, $-\mathrm{i}\gamma$, and the η couplings in real time.

The structure of one actuator is detailed in Fig. 2(a). This is an electrodynamic loudspeaker within a closed cavity, which features a diaphragm mechanically driven by a voice coil, placed in a permanent magnetic field. At low frequencies, the loudspeaker can be approximated as a mass-spring-damper system, and the diaphragm motion at small displacements can be described in the Laplace domain by[43,44]

$$Z_{mo}(s)v(s) = -S_d p(s) + Bli(s), \tag{7a}$$
$$u(s) = Z_{eb}(s)i(s) + Blv(s). \tag{7b}$$

Here, $Z_{mo}(s) = M_{ms}s + R_{ms} + \frac{1}{C_{ms}s}$ and $Z_{eb}(s) = L_e s + R_e$ are, respectively, the open circuit mechanical and the blocked electrical impedance of the loudspeaker, where M_{ms}, R_{ms}, and C_{mc} represent its moving mass, mechanical damping, and the total mechanical compliance. S_d is the effective area of the diaphragm, with p being the total sound pressure acting on it, which includes both the incident and scattered pressure. v is the vibration velocity of the speaker diaphragm, i is the current in the voice coil, and u is the input voltage between the electrical terminals. Bl is the force factor of the speaker, where B is the magnetic field strength and l is the length of the voice coil in the magnetic field. R_e is the DC resistance, and L_e is the self-inductance of the voice coil. To avoid the impact of the coil inductance L_e on the system stability, we designed

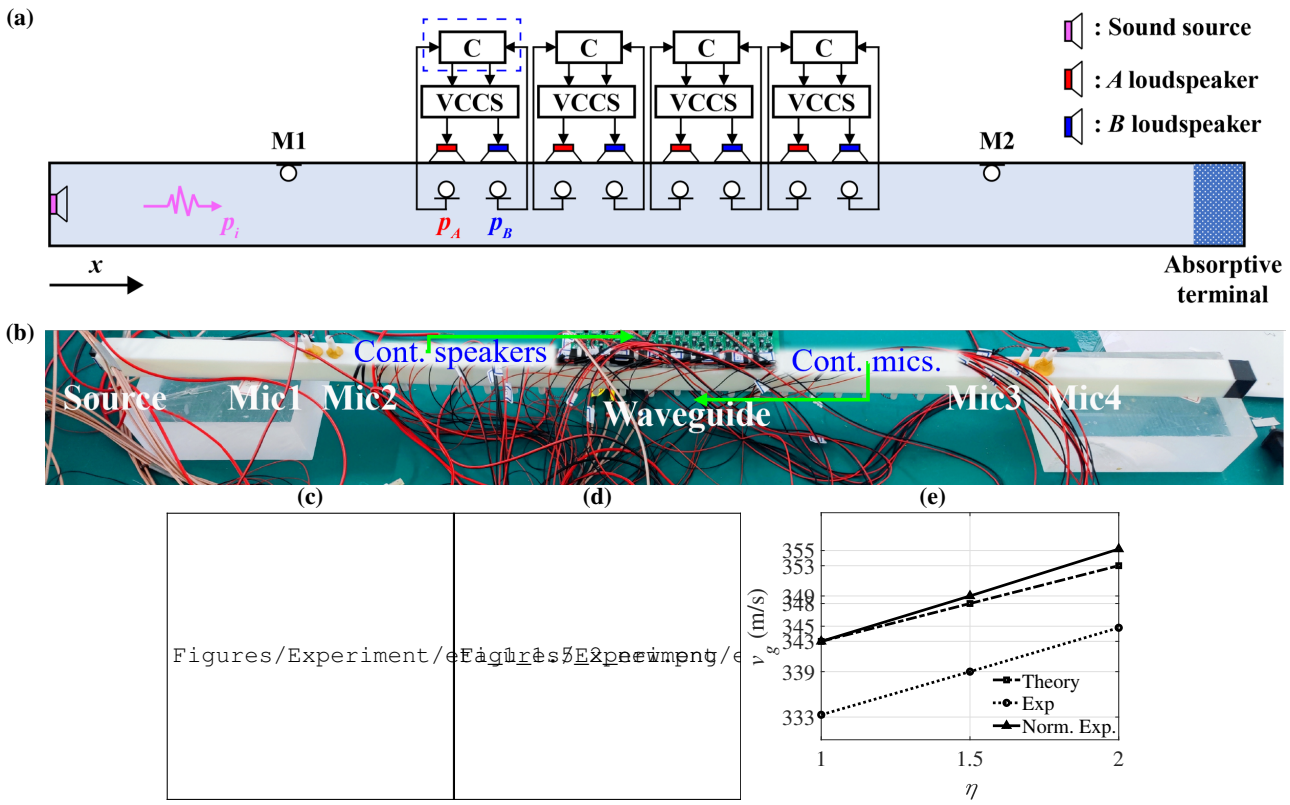

FIG. 3. Experimental demonstration of accelerated wave packet propagation. (a) Schematic of the experimental setup. (b) Photograph of the waveguide, comprising 8 active sites. (c) The measured waveform at microphone Mic4 relative to microphone Mic1 as a function of time for $\eta = 1$, black, $\eta = 1.5$, purple, and $\eta = 2$, green. (d) Zoom-in of the measured waveform in (c). (e) Comparison of the calculated group velocities with the measured results. Dashed - the theoretical values obtained from Eq. (6). Dotted - the measured values. Solid - the measured values normalized by the Hermitian velocity of 343 m/s.

our loudspeakers to be driven by current sources. We set the control law in each unit cell to

$$i^{A/B}(s) = (G_S \pm sG_\gamma)p^{A/B}(s) + G_\eta \left[p^{B/A}(s) - p^{A/B}(s)\right], \tag{8}$$

which results in the acoustic velocity commands

$$\begin{aligned} v^{A/B}(s) = &\frac{-S_d + Bl(G_S \pm sG_\gamma)}{Z_{mo}(s)} p^{A/B}(s) \\ &+ \frac{BlG_\eta}{Z_{mo}(s)} \left[p^{B/A}(s) - p^{A/B}(s)\right]. \end{aligned} \tag{9}$$

Comparing Eq. (9) with Eq. (4), and assuming $Z_{mo}(s) \approx M_{ms}s$ in our working frequency range, the controller gains take the form

$$G_S = \frac{S_d}{Bl},\ G_\gamma = \frac{\gamma M_{ms}}{Blz_0},\ G_\eta = \frac{(\eta-1)M_{ms}}{\rho_0 aBl}. \tag{10}$$

The structure of the control law in Eq. (8) with Eq. (10) is schematically illustrated in Fig. 2(b). The gain G_S is responsible for the cancellation of the internal physical feedback of the loudspeaker, whereas G_γ and G_η create the γ and the η couplings, respectively. We then demonstrate the performance of our controlled waveguide using a numerical experiment. We calculate the controller gains for the cases $\eta = 1.5, 2, 3$, for which the corresponding values of $\gamma = 0.16, 0.31, 0.60$ are numerically obtained from Eq. (6) for $\mu = 1, 1.055, 1.161$. The dispersion relations of the resulting closed loop, calculated at low frequencies by PWE, are depicted in Fig. 2(c), on top of the uncontrolled case $\eta = 1, \gamma = 0$. The spectrum slope increases with γ, indicating the expected increase in group velocity.

A waveguide controlled by the feedback system in Fig. 2(a)-(b) for the above combinations of γ, η, was then simulated in the time domain using FE (with filters added to enhance stability, see App. D). The simulated responses to a Gaussian wave packet are given in Fig. 2(d). The group velocities calculated from these responses are depicted in Fig. 2(e) by circles. The numerical results fit well the analytical expression Eq. (6), depicted by a curve.

IV. EXPERIMENTAL DEMONSTRATION

To confirm the group velocity increase, an active metastructure was fabricated, as shown in the schematic in Fig. 3(a), and the photograph in Fig. 3(b). The sound source is positioned at the left end of the waveguide, whereas the right end contains glass wool for sound wave absorption, sealed by a 4 mm thick resin block. The waveguide has a uniform wall thickness of 4 mm, produced via 3D printing using a resin material with a density of 1180 kg/m^3. The waveguide has

a length of 1 m and a square cross-section with dimensions of 15×15 mm^2, corresponding to a cutoff frequency for the plane wave mode of 11467 Hz. The active metamaterial, 20 cm in total length, consists of four unit cells (8 active sites) positioned in the center of the waveguide. Each unit cell, measuring $a = 5$ cm, contains two identical loudspeakers on the top and two identical microphones on the bottom. Two additional microphones, Mic1 and Mic4, are symmetrically positioned on the left and right sides of the active metamaterial, spaced 60 cm apart, to monitor the velocity of acoustic wave propagation. A controller corresponding to Fig. 2(b) was designed to regulate the output of the control sources A and B. This was realized using voltage-controlled current sources (VCCS), which convert a voltage signal into a proportional current signal (with unity gain) to drive the loudspeakers, as detailed in App. E. The output voltage signals of the controller, u_{oA} and u_{oB}, are therefore converted into current signals, i.e., $i^{A/B} = u^{A/B}$.

To ensure consistency between the loudspeakers and microphones, careful selections and calibrations were performed. The Thiele & Small parameters of the loudspeakers were measured using the Klippel electroacoustic test system. The following average parameters were obtained: the diaphragm mass $M_{ms} = 0.0689$ g, the force factor $Bl = 0.606$ N/A, the effective diaphragm area $S_d = 72$ mm^2, leading to $\beta = 0.32$, and the resonance frequency 900 Hz. Electret condenser microphones were used as the pressure sensors. The microphone signals were amplified to ensure a sensitivity of $S_0 = 400$ mV/Pa. The controller was designed using analog circuitry and fabricated using a printed circuit board[45]. Potentiometers were used to adjust G_γ and G_η to achieve the desired different values of γ and η according to Eq. (10), divided by S_0. An NI acquisition card with a sampling rate of $f_s = 200$ kHz was used to record the microphone signals from Mic1 and Mic4.

The signal supplied to the sound source was a Gaussian pulse modulated by a 2500 Hz sine wave. Three sets of measurements were conducted with $\eta = 1$, 1.5, and 2, respectively, and the corresponding γ was calculated from Eq. (6) to be 0, 0.16, and 0.29. The measurement results are presented in Fig. 3(c), with a close-up in Fig. 3(d). These results compare the pulse waveform over time for the Hermitian case $\gamma = 0$, $\eta = 1$ (black) with the non-Hermitian cases $\eta = 1.5$ (purple) and $\eta = 2$ (green). Setting the peak time of the pulse recorded by microphone Mic1 as 0, the peak arrival times at microphone Mic4 are advanced by $\delta_t = 0.01$ ms and $\delta_t = 0.02$ ms for $\eta = 1.5$ and $\eta = 2$, respectively. This confirms that the acoustic wave speed was increased in the designed active metamaterial.

The group velocity v_g of the sound wave in the metamaterial can be determined by the equation $\frac{l}{c} - \frac{l}{v_g} = \delta_t$, where $l = 20$ cm is the total length of the active metamaterial. The baseline speed c can be obtained as 333 m/s by measurement at the room temperature of 20 °C, i.e., $c = s/t_0$, where $s = 60$ cm denotes the distance between microphones Mic1 and Mic4, and $t_0 = 1.8$ ms is the time difference between the pulse arriving at Mic4 and Mic1 in the Hermitian case. Therefore, for the non-Hermitian cases $\eta = 1.5$ and $\eta = 2$, the sound wave velocities in the active metamaterial are 339 m/s and 345 m/s, respectively. Fig. 3(e) compares experimental and theoretical results. The discrepancy between the theoretical and experimental results is attributed to the measured baseline sound velocity $c = 333$ m/s being lower than the actual value of 343 m/s at room temperature. This deviation primarily stems from measurement errors, including thermoviscous boundary layer effects slowing down the sound velocity, a misalignment between the acoustic and physical centers of microphones Mic1 and Mic4, and thermal deformation of the waveguide structure. Taking the actual room temperature sound speed $c = 343$ m/s, the corrected experimental results become $v_g = 349$ m/s for $\eta = 1.5$ and $v_g = 355$ m/s for $\eta = 2$. These corrected values, shown as the solid line in Fig. 3(e), align closely with the theoretical results.

V. DISCUSSION AND CONCLUSION

To conclude, we have designed an acoustic waveguide system that supports wave propagation at group velocities higher than the speed of sound. The velocity increase was obtained via active couplings, which were created by acoustic transducers, discretely spaced and attached to the waveguide wall. Current-driven loudspeakers enabled real-time control of the acoustic field via sound pressure measurements, acquired by microphones at the opposite wall.The measurements were processed by the controllers to realize an onsite gain/loss γ, and inter-site coupling η, related by Eq.(6). This relation was modified from lattice systems to address the challenge of merging a spatially discrete coupling pattern into the continuous waveguide medium, achieving the desired dynamics while maintaining stability. The stability was manifested by the real spectrum of the resulting PT-symmetric non-Hermitian system, with the group velocity growth proportional to the square root of γ. FE and PWE simulations suggested that, theoretically, the waveguide system was stable for all the achieved group velocities. In our experiment, we managed to maintain stable propagation for a velocity increase of up to 355 m/s from the nominal 343 m/s, and this limit can be further pushed by optimizations of the control setup and algorithm.

Our active coupling approach is advantageous in applications that forbid waveguide cross-section blocking, and/or require long-range coupling between multiple active cells. Compared to purely passive PT-symmetric systems, the active approach expands the utility of the parameter space and could achieve unique functionalities that are otherwise not possible without injecting external energy. More importantly, since the onsite potential and coupling are realized by acoustic transducers and a feedback control scheme, the modulation profile is not restricted to a PT-symmetric regime demonstrated in this work. We anticipate the platform to be easily configured and more complex interactions, including on-demand nonlocal effects, can be synthesized, which could lead to other novel wave properties. The stable operation also offers great flexibility in its real-world applications. Finally, the real-time feedback system offers dynamic tuning of the wave response, which is difficult to achieve using passive structures. It is hoped that our active metamaterial platform and experimen-

tal demonstration of supersonic wave propagation will pave the way for new complex wave-guiding capabilities.

ACKNOWLEDGEMENTS

K. W., H. Z., and J. L. have been supported by the National Natural Science Foundation of China (grant no. 12274221). F. L. has been partially supported by the UK's Engineering and Physical Sciences Research Council (EPSRC) through the 3rd funding call by the UK Acoustics Network Plus EP/V007866/1. C.S. acknowledges support from the National Science Foundation under Grant No. ECCS-2337069. L.S. was partially supported by the Israel Science Foundation Grants No. 2177/23 and 2876/23.

Appendix A: Group velocity control in the lattice model

The analogous lattice model in Fig. 1(b) is represented by the augmented eigenvalue problem in (2), which reads

$$\Omega^4 - \left(2(1+\eta) - \gamma^2\right)\Omega^2 + (1+\eta)^2 - ff^\dagger = 0. \quad \text{(S1)}$$

Its solution is given by

$$\Omega^2 = \tfrac{1}{2}\left(2(1+\eta) - \gamma^2\right) \pm \tfrac{1}{2}\sqrt{\delta}, \quad \text{(S2)}$$

with

$$\delta = \left(2(1+\eta) - \gamma^2\right)^2 - 4\left((1+\eta)^2 - ff^\dagger\right). \quad \text{(S3)}$$

The requirements for real spectrum (with minimum at $\cos ka = -1$), therefore become gives the PT symmetry condition $\gamma \leq \gamma^*$ of Eq. (6). We then obtain $(1+\eta)^2 - ff^\dagger = 2\eta(1-\cos ka)$, $\delta = 8\eta(1+\cos ka)$, and the dispersion relation of (S2), as well as the corresponding normalized group velocity, read

$$\Omega = \frac{\omega}{\omega_0} = \sqrt{\sqrt{2}\gamma^* + 2}\cdot\sqrt{1 \pm \sqrt{\tfrac{1}{2}\left(1+\cos ka\right)}}, \quad \text{(S4)}$$

and

$$\frac{v_g}{\omega_0} = \frac{\partial\Omega}{\partial ka} = \frac{1}{4}\frac{\sin ka}{\sqrt{1+\cos ka}}\frac{\sqrt{\gamma^* + \sqrt{2}}}{\sqrt{\sqrt{2} \pm \sqrt{1+\cos ka}}}. \quad \text{(S5)}$$

Since in the Hermitian system ($\gamma = 0$, $a \to \frac{a}{2}$) we have

$$\Omega_H = \sqrt{2\left(1-\cos ka\right)}, \quad \text{(S6)}$$

and

$$\frac{v_0}{\omega_0} = \frac{\sin\frac{ka}{2}}{2\sqrt{2\left(1-\cos\frac{ka}{2}\right)}}, \quad \text{(S7)}$$

the ratio between the non-Hermitian and Hermitian group velocities, (S5) and (S7), becomes

$$\frac{v_g}{v_0} = \sqrt{\frac{1}{\sqrt{2}}\gamma^* + 1}, \quad \text{(S8)}$$

and is independent of k.

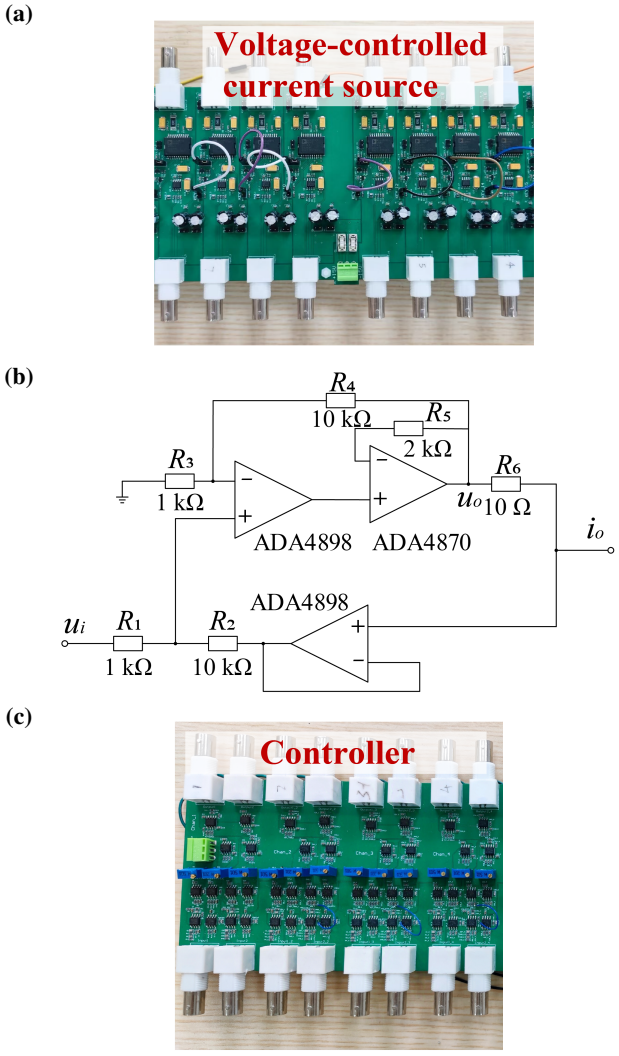

FIG. S1. Realization of the controller of Fig. 2(b). (a),(b) Photograph and circuitry of the Voltage-Controlled Current Sources. (c) Photograph of the controller.

Appendix B: Group velocity control in the waveguide

Mechanical - electric - acoustic circuits analogy?

Appendix C: The Plane Wave Expansion derivation

We substitute the proposed solution $p(x,t) = \mathrm{e}^{-\mathrm{i}\omega t}P(x)$, with $P(x) = \sum_{m=-M}^{M}\mathrm{e}^{\mathrm{i}(k+m)\mathbf{b}_1\cdot x\mathbf{d}_1}\overline{p}$, $\mathbf{b}_1 = \frac{2\pi}{a}\hat{\mathbf{e}}_1$ and $\mathbf{d}_1 = a\hat{\mathbf{e}}_1$, into the n_{th} unit cell of (5). Using a more general formulation $\mathbf{r} = x\mathbf{d}_1$, $\mathbf{k} = k\mathbf{b}_1$, and $\mathbf{G} = m\mathbf{b}_1$, and acknowledging that p_{tt}, p_t transform to frequency domain as

$-\omega^2 p$, $\mathrm{i}\omega p$, we obtain

$$\begin{aligned}
&\rho_0\omega^2 \sum_{m=-M}^{M} e^{-\mathrm{i}(\mathbf{k}+\mathbf{G})\cdot\mathbf{r}}\overline{p} = \sum_{m=-M}^{M} b_0|\mathbf{k}+\mathbf{G}|^2 e^{-\mathrm{i}(\mathbf{k}+\mathbf{G})\cdot\mathbf{r}}\overline{p} \\
&-\beta \sum_{m=-M}^{M} \Big[b_0\frac{\eta-1}{a}\left(e^{-\mathrm{i}(\mathbf{k}+\mathbf{G})\cdot\mathbf{R}_B} - e^{-\mathrm{i}(\mathbf{k}+\mathbf{G})\cdot\mathbf{R}_A}\right) \\
&+\gamma z_0 \mathrm{i}\omega e^{-\mathrm{i}(\mathbf{k}+\mathbf{G})\cdot\mathbf{R}_A}\Big]\delta(\mathbf{r}-\mathbf{R}_A)\overline{p} \\
&-\beta \sum_{m=-M}^{M} \Big[b_0\frac{\eta-1}{a}\left(e^{-\mathrm{i}(\mathbf{k}+\mathbf{G})\cdot\mathbf{R}_A} - e^{-\mathrm{i}(\mathbf{k}+\mathbf{G})\cdot\mathbf{R}_B}\right) \\
&-\gamma z_0 \mathrm{i}\omega e^{-\mathrm{i}(\mathbf{k}+\mathbf{G})\cdot\mathbf{R}_B}\Big]\delta(\mathbf{r}-\mathbf{R}_B)\overline{p},
\end{aligned} \tag{S1}$$

where $\mathbf{R}_A = -\frac{a}{4}\mathbf{d}_1$ and $\mathbf{R}_B = \frac{a}{4}\mathbf{d}_1$ are the actuators locations measured from the center of the unit cell. Multiplying (S1) by $e^{\mathrm{i}(\mathbf{k}+\widehat{\mathbf{G}})\cdot\mathbf{r}}$, where $\widehat{\mathbf{G}} = \widehat{m}\mathbf{b}_1$ for $\widehat{m} \neq m$, gives

$$\begin{aligned}
&\rho_0\omega^2 \sum_{m=-M}^{M} e^{-\mathrm{i}(\mathbf{G}-\widehat{\mathbf{G}})\cdot\mathbf{r}}\overline{p} = \sum_{m=-M}^{M} b_0|\mathbf{k}+\mathbf{G}|^2 e^{-\mathrm{i}(\mathbf{G}-\widehat{\mathbf{G}})\cdot\mathbf{r}}\overline{p} \\
&-\beta \sum_{m=-M}^{M} e^{\mathrm{i}(\mathbf{k}+\widehat{\mathbf{G}})\cdot\mathbf{r}}\Big(b_0\frac{\eta-1}{a}\left[e^{-\mathrm{i}(\mathbf{k}+\mathbf{G})\cdot\mathbf{R}_B} - e^{-\mathrm{i}(\mathbf{k}+\mathbf{G})\cdot\mathbf{R}_A}\right] \\
&+\gamma z_0 \mathrm{i}\omega e^{-\mathrm{i}(\mathbf{k}+\mathbf{G})\cdot\mathbf{R}_A}\Big)\delta(\mathbf{r}-\mathbf{R}_A)\overline{p} \\
&-\beta \sum_{m=-M}^{M} e^{\mathrm{i}(\mathbf{k}+\widehat{\mathbf{G}})\cdot\mathbf{r}}\Big(b_0\frac{\eta-1}{a}\left[e^{-\mathrm{i}(\mathbf{k}+\mathbf{G})\cdot\mathbf{R}_A} - e^{-\mathrm{i}(\mathbf{k}+\mathbf{G})\cdot\mathbf{R}_B}\right] \\
&-\gamma z_0 \mathrm{i}\omega e^{-\mathrm{i}(\mathbf{k}+\mathbf{G})\cdot\mathbf{R}_B}\Big)\delta(\mathbf{r}-\mathbf{R}_B)\overline{p}.
\end{aligned} \tag{S2}$$

Due to the orthogonality of the Fourier series, we have

$$\int_{A_c} e^{-\mathrm{i}(\mathbf{G}-\widehat{\mathbf{G}})\cdot\mathbf{r}}\mathrm{d}A_c = \begin{cases} A_c, & \mathbf{G} = \widehat{\mathbf{G}} \\ 0, & \mathbf{G} \neq \widehat{\mathbf{G}} \end{cases} \tag{S3}$$

$$\int_{A_c} f(\mathbf{r})\delta(\mathbf{r}-\mathbf{R}_\alpha)\mathrm{d}A_c = f(\mathbf{R}_\alpha), \tag{S4}$$

where $A_c = a$ is the unit cell length and the lattice constant. Integrating (S2) over a unit cell then gives

$$\begin{aligned}
\rho_0\omega^2 a\widehat{p} &= b_0|\mathbf{k}+\widehat{\mathbf{G}}|^2 a\widehat{p} \\
&-\beta\Big(b_0\frac{\eta-1}{a}e^{\mathrm{i}\mathbf{k}\cdot(\mathbf{R}_A-\mathbf{R}_B)}e^{\mathrm{i}\widehat{\mathbf{G}}\cdot\mathbf{R}_A}e^{-\mathrm{i}\mathbf{G}\cdot\mathbf{R}_B}\widehat{p} \\
&-\left[b_0\frac{\eta-1}{a} - \gamma z_0\mathrm{i}\omega\right]e^{-\mathrm{i}(\mathbf{G}-\widehat{\mathbf{G}})\cdot\mathbf{R}_A}\widehat{p}\Big) \\
&-\beta\Big(b_0\frac{\eta-1}{a}e^{\mathrm{i}\mathbf{k}\cdot(\mathbf{R}_B-\mathbf{R}_A)}e^{\mathrm{i}\widehat{\mathbf{G}}\cdot\mathbf{R}_B}e^{-\mathrm{i}\mathbf{G}\cdot\mathbf{R}_A}\widehat{p} \\
&-\left[b_0\frac{\eta-1}{a} + \gamma z_0\mathrm{i}\omega\right]e^{-\mathrm{i}(\mathbf{G}-\widehat{\mathbf{G}})\cdot\mathbf{R}_B}\widehat{p}\Big),
\end{aligned} \tag{S5}$$

where $\mathbf{G}\cdot\mathbf{R}_A = -\frac{\pi}{2}m$, and $\mathbf{G}\cdot\mathbf{R}_B = \frac{\pi}{2}m$. Using matrix formulation, we define $\sum_{m=-M}^{M} e^{\mathrm{i}\widehat{\mathbf{G}}\cdot\mathbf{R}_{\widehat{\jmath}}}e^{-\mathrm{i}\mathbf{G}\cdot\mathbf{R}_j}\widehat{\mathbf{p}} = E_{\widehat{\jmath}j}\widehat{\mathbf{p}}$, where

$$E_{\widehat{\jmath}j} = e^{\mathrm{i}\left[\begin{array}{cccc}\mathbf{G}_1 & \mathbf{G}_2 & \cdots & \mathbf{G}_N\end{array}\right]'\cdot\mathbf{R}_{\widehat{\jmath}}}\cdot e^{-\mathrm{i}\mathbf{R}_j\cdot\left[\begin{array}{cccc}\mathbf{G}_1 & \mathbf{G}_2 & \cdots & \mathbf{G}_N\end{array}\right]} \tag{S6}$$

and $N = 2M+1$ is the total number of terms in the series. Eq. (S5) then takes the form of the polynomial eigenvalue problem

$$\left(\mathbf{q}_2\omega^2 + \mathbf{q}_1\omega + \mathbf{q}_0\right)\widehat{\mathbf{p}} = 0, \tag{S7}$$

where

$$\begin{aligned}
\mathbf{q}_2 &= \rho_0 a\mathbf{I}_N, \\
\mathbf{q}_1 &= \beta\gamma z_0\mathrm{i}\left(E_{\widehat{A}A} - E_{\widehat{B}B}\right), \\
\mathbf{q}_0 &= -b_0 a\begin{pmatrix}|\mathbf{k}+\widehat{\mathbf{G}}_1|^2 & & \\ & \cdots & \\ & & |\mathbf{k}+\widehat{\mathbf{G}}_N|^2\end{pmatrix} \\
&+\beta b_0\frac{\eta-1}{a}\Big(e^{\mathrm{i}\mathbf{k}\cdot(\mathbf{R}_A-\mathbf{R}_B)}E_{\widehat{A}B} - E_{\widehat{A}A} \\
&+e^{\mathrm{i}\mathbf{k}\cdot(\mathbf{R}_B-\mathbf{R}_A)}E_{\widehat{B}A} - E_{\widehat{B}B}\Big).
\end{aligned} \tag{S8}$$

We then rewrite (S7)-(S8) in a companion form to obtain an augmented linear eigenvalue problem

$$\omega\mathbf{P}\mathbf{v} = \mathbf{Q}\mathbf{v}, \tag{S9}$$

where $\mathbf{v}$ is the augmented eigenvector of length $2N$, and

$$\mathbf{P} = \begin{pmatrix}\mathbf{I} & 0 \\ 0 & \mathbf{q}_2\end{pmatrix}, \quad \mathbf{Q} = \begin{pmatrix}0 & \mathbf{I} \\ -\mathbf{q}_0 & -\mathbf{q}_1\end{pmatrix}. \tag{S10}$$

The solution of (S9)-(S10) gives the black and orange dispersion curves in Fig. 1(g)-(j).

Appendix D: The Finite Element scheme details

The FE model included low pass filters of the form...

Appendix E: The controller structure

The VCCS employed in our experiment, photographed in Fig. S1(a), were designed using an improved Howland current pump circuit[46]. It integrates the high output of the operational amplifier ADA4870 with the fast response of the operational amplifier ADA4898. The relation between the output current i_o and the input voltage u_i then becomes $i_o = \frac{R_2}{R_1R_6}u_i + \frac{R_2R_3-R_1R_4}{R_1R_6(R_3+R_4)}u_o$, as illustrated in Fig. S1(b). Substituting the resistor values from Fig. S1(b) yields the output current $i_o = u_i$. The circuit performance was verified via Multisim simulations. The resulting controller is photographed in Fig. S1(c).

* f.langfeldt@soton.ac.uk
† lujing@nju.edu.cn
‡ leabeilkin@tauex.tau.ac.il

[1] Y. Ashida, Z. Gong, and M. Ueda, "Non-Hermitian physics," *Advances in Physics*, vol. 69, no. 3, pp. 249–435, 2020.
[2] K. Ding, C. Fang, and G. Ma, "Non-Hermitian topology and exceptional-point geometries," *Nature Reviews Physics*, vol. 4, no. 12, pp. 745–760, 2022.
[3] R. El-Ganainy, K. G. Makris, M. Khajavikhan, Z. H. Musslimani, S. Rotter, and D. N. Christodoulides, "Non-Hermitian physics and PT symmetry," *Nature Physics*, vol. 14, no. 1, pp. 11–19, 2018.
[4] M.-A. Miri and A. Alu, "Exceptional points in optics and photonics," *Science*, vol. 363, no. 6422, p. eaar7709, 2019.
[5] C. M. Bender and S. Boettcher, "Real spectra in non-Hermitian Hamiltonians having PT symmetry," *Physical Review Letters*, vol. 80, no. 24, p. 5243, 1998.
[6] C. M. Bender, "Making sense of non-Hermitian Hamiltonians," *Reports on Progress in Physics*, vol. 70, no. 6, p. 947, 2007.
[7] H. Zhao and L. Feng, "Parity-time symmetric photonics," *National Science Review*, vol. 5, no. 2, pp. 183–199, 2018.
[8] L. Feng, Z. J. Wong, R.-M. Ma, Y. Wang, and X. Zhang, "Single-mode laser by parity-time symmetry breaking," *Science*, vol. 346, no. 6212, pp. 972–975, 2014.
[9] H. Hodaei, A. U. Hassan, S. Wittek, H. Garcia-Gracia, R. El-Ganainy, D. N. Christodoulides, and M. Khajavikhan, "Enhanced sensitivity at higher-order exceptional points," *Nature*, vol. 548, no. 7666, pp. 187–191, 2017.
[10] Z. Lin, H. Ramezani, T. Eichelkraut, T. Kottos, H. Cao, and D. N. Christodoulides, "Unidirectional invisibility induced by PT-symmetric periodic structures," *Physical Review Letters*, vol. 106, no. 21, p. 213901, 2011.
[11] D. L. Sounas, R. Fleury, and A. Alù, "Unidirectional cloaking based on metasurfaces with balanced loss and gain," *Physical Review Applied*, vol. 4, no. 1, p. 014005, 2015.
[12] X. Zhu, H. Ramezani, C. Shi, J. Zhu, and X. Zhang, "PT-symmetric acoustics," *Physical Review X*, vol. 4, no. 3, p. 031042, 2014.
[13] C. Shi, M. Dubois, Y. Chen, L. Cheng, H. Ramezani, Y. Wang, and X. Zhang, "Accessing the exceptional points of parity-time symmetric acoustics," *Nature Communications*, vol. 7, no. 1, p. 11110, 2016.
[14] T. Liu, X. Zhu, F. Chen, S. Liang, and J. Zhu, "Unidirectional wave vector manipulation in two-dimensional space with an all passive acoustic parity-time-symmetric metamaterials crystal," *Physical Review Letters*, vol. 120, no. 12, p. 124502, 2018.
[15] X. Wang, X. Fang, D. Mao, Y. Jing, and Y. Li, "Extremely asymmetrical acoustic metasurface mirror at the exceptional point," *Physical Review Letters*, vol. 123, no. 21, p. 214302, 2019.
[16] K. Stojanoska and C. Shen, "Non-Hermitian planar elastic metasurface for unidirectional focusing of flexural waves," *Applied Physics Letters*, vol. 120, no. 24, 2022.
[17] R. Cai, Y. Jin, Y. Li, J. Zhu, H. Zhu, T. Rabczuk, and X. Zhuang, "Absorption-lasing effects and exceptional points in parity-time symmetric non-Hermitian metaplates," *Journal of Sound and Vibration*, vol. 555, p. 117710, 2023.
[18] L. Huang, S. Huang, C. Shen, S. Yves, A. S. Pilipchuk, X. Ni, S. Kim, Y. K. Chiang, D. A. Powell, J. Zhu *et al.*, "Acoustic resonances in non-Hermitian open systems," *Nature Reviews Physics*, vol. 6, no. 1, pp. 11–27, 2024.
[19] S. Xia, D. Kaltsas, D. Song, I. Komis, J. Xu, A. Szameit, H. Buljan, K. G. Makris, and Z. Chen, "Nonlinear tuning of PT symmetry and non-Hermitian topological states," *Science*, vol. 372, no. 6537, pp. 72–76, 2021.
[20] A. Stegmaier, S. Imhof, T. Helbig, T. Hofmann, C. H. Lee, M. Kremer, A. Fritzsche, T. Feichtner, S. Klembt, S. Höfling *et al.*, "Topological defect engineering and PT symmetry in non-Hermitian electrical circuits," *Physical Review Letters*, vol. 126, no. 21, p. 215302, 2021.
[21] Y. Li, C. Liang, C. Wang, C. Lu, and Y.-C. Liu, "Gain-loss-induced hybrid skin-topological effect," *Physical Review Letters*, vol. 128, no. 22, p. 223903, 2022.
[22] B. Hu, Z. Zhang, H. Zhang, L. Zheng, W. Xiong, Z. Yue, X. Wang, J. Xu, Y. Cheng, X. Liu *et al.*, "Non-Hermitian topological whispering gallery," *Nature*, vol. 597, no. 7878, pp. 655–659, 2021.
[23] R. Pernas-Salomón, L.-Y. Zheng, Z. Zhang, P. Gao, X. Liu, Y. Cheng, and J. Christensen, "Theory of non-Hermitian topological whispering gallery," *npj Computational Materials*, vol. 8, no. 1, p. 241, 2022.
[24] Y. Aurégan and V. Pagneux, "PT-symmetric scattering in flow duct acoustics," *Physical Review Letters*, vol. 118, no. 17, p. 174301, 2017.
[25] J. Christensen, M. Willatzen, V. Velasco, and M.-H. Lu, "Parity-time synthetic phononic media," *Physical Review Letters*, vol. 116, no. 20, p. 207601, 2016.
[26] W.-J. Yang, Z.-Z. Yang, A.-Y. Guan, X.-Y. Zou, and J.-C. Cheng, "Design and experimental demonstration of effective acoustic gain medium for PT-symmetric refractive index," *Applied Physics Letters*, vol. 120, no. 6, 2022.
[27] L. Zhang, Y. Yang, Y. Ge, Y.-J. Guan, Q. Chen, Q. Yan, F. Chen, R. Xi, Y. Li, D. Jia *et al.*, "Acoustic non-Hermitian skin effect from twisted winding topology," *Nature Communications*, vol. 12, no. 1, pp. 1–7, 2021.
[28] K. Wang, L. Shi, H. Zou, S. Zhao, C. Shen, and J. Lu, "A broadband active sound absorber with adjustable absorption coefficient and bandwidth," *The Journal of the Acoustical Society of America*, vol. 156, no. 2, pp. 1048–1057, 2024.
[29] R. Fleury, D. Sounas, and A. Alu, "An invisible acoustic sensor based on parity-time symmetry," *Nature Communications*, vol. 6, no. 1, p. 5905, 2015.
[30] A. Maddi, V. Pagneux, and V. Achilleos, "Exact analog of the Hatano-Nelson model in one-dimensional continuous nonreciprocal systems," *Physical Review Research*, vol. 6, no. 1, p. L012061, 2024.
[31] A. Szameit, M. C. Rechtsman, O. Bahat-Treidel, and M. Segev, "PT-symmetry in honeycomb photonic lattices," *Physical Review A*, vol. 84, no. 2, p. 021806, 2011.
[32] Y. Benisty, S. Jana, and L. Sirota, "Controlled fast wavepackets in non-Hermitian lattices," *arXiv preprint arXiv:2407.10289*, 2024.
[33] T. Hofmann, T. Helbig, C. H. Lee, M. Greiter, and R. Thomale, "Chiral voltage propagation and calibration in a topolectrical Chern circuit," *Physical Review Letters*, vol. 122, no. 24, p. 247702, 2019.
[34] M. I. Rosa and M. Ruzzene, "Dynamics and topology of non-Hermitian elastic lattices with non-local feedback control interactions," *New Journal of Physics*, vol. 22, no. 5, p. 053004, 2020.
[35] T. Helbig, T. Hofmann, S. Imhof, M. Abdelghany, T. Kiessling, L. Molenkamp, C. Lee, A. Szameit, M. Greiter, and R. Thomale, "Generalized bulk–boundary correspondence in non-Hermitian topolectrical circuits," *Nature Physics*, vol. 16, no. 7, pp. 747–750, 2020.
[36] S. Jana and L. Sirota, "Gravitational lensing and tunneling of mechanical waves in synthetic curved spacetime," *Physical Review*

Research, vol. 5, no. 3, p. 033104, 2023.

[37] P. Zhu, X.-Q. Sun, T. L. Hughes, and G. Bahl, "Higher rank chirality and non-Hermitian skin effect in a topolectrical circuit," *Nature Communications*, vol. 14, no. 1, p. 720, 2023.

[38] F. Langfeldt and J. Cheer, "Controlling the effective surface mass density of membrane-type acoustic metamaterials using dynamic actuators," *The Journal of the Acoustical Society of America*, vol. 153, no. 2, pp. 961–961, 2023.

[39] X. Wen, H. K. Yip, C. Cho, J. Li, and N. Park, "Acoustic amplifying diode using nonreciprocal Willis coupling," *Physical Review Letters*, vol. 130, no. 17, p. 176101, 2023.

[40] D. Halder, R. Thomale, and S. Basu, "Circuit realization of a two-orbital non-Hermitian tight-binding chain," *Physical Review B*, vol. 109, no. 11, p. 115407, 2024.

[41] D. A. Kovacevich, K. Grosh, and B.-I. Popa, "Stability-derived bounds on the realizable acoustic properties of active metamaterials," *Physical Review Applied*, vol. 21, no. 5, p. L051002, 2024.

[42] R. Chaunsali, C.-W. Chen, and J. Yang, "Subwavelength and directional control of flexural waves in zone-folding induced topological plates," *Physical Review B*, vol. 97, no. 5, p. 054307, 2018.

[43] E. Rivet, S. Karkar, and H. Lissek, "Broadband low-frequency electroacoustic absorbers through hybrid sensor-/shunt-based impedance control," *IEEE Transactions on Control Systems Technology*, vol. 25, no. 1, pp. 63–72, 2016.

[44] N. Geib, A. Sasmal, Z. Wang, Y. Zhai, B.-I. Popa, and K. Grosh, "Tunable nonlocal purely active nonreciprocal acoustic media," *Physical Review B*, vol. 103, no. 16, p. 165427, 2021.

[45] "Supplementary material."."

[46] I. V. Lam, "Analysis of improved Howland current pump configurations," *Tex. Instrum*, 2023.